Article
Vol. 26, No. 1, p. 151–165, February 2022
https://doi.org/10.1007/s12303-021-0013-7
pISSN 1226-4806 eISSN 1598-7477
Geosciences Journal GJ

Fracture behavior of cylindrical sandstone specimens with two pre-existing flaws: experimental investigation and PFC3D simulation

Yan-Hua Huang[1,2], Sheng-Qi Yang[1], Guo-Qing Chen[2]*, and Bo Meng[1]

[1]State Key Laboratory for Geomechanics and Deep Underground Engineering, School of Mechanics and Civil Engineering, China University of Mining and Technology, Xuzhou 221116, China
[2]State Key Laboratory of Geohazard Prevention and Geoenvironment Protection, Chengdu University of Technology, Chengdu 610059, China

ABSTRACT: It is important to analyze the rock crack initiation, propagation and coalescence in fractured rock mass. At present, the 3D crack evolution process of pre-flawed rock has not been comprehensively studied during the deformation. In this study, uniaxial compression tests were carried out on cylindrical sandstone specimens with two pre-existing flaws with various ligament inclination angles. The crack evolution process at the front surface of the specimen was analyzed by photographic and AE monitoring. In addition, a 3D discrete element modelling was conducted to explore the spatial crack evolution behaviors during compressive loading. Both the numerical strength and final failure modes of specimens were consistent with those obtained in the laboratory experiment. The numerical simulation results revealed that the internal crack distribution was not always identical along the thickness direction. Two types of crack coalescence were identified. The experimental and numerical results enhance the understanding of 3D crack evolution mechanism of fractured rock under external loading.

Key words: rock mechanics, crack coalescence, 3D fracture, peak strength, discrete element modelling

Manuscript received January 11, 2021; Manuscript accepted April 16, 2021

1. INTRODUCTION

Crack initiation, propagation and coalescence are common in rock mass under external loads. Generally, cracks could reduce the strength and stiffness of rock mass. Many instability failure accidents of rock engineering occur due to the crack nucleation and growth, such as the step-path failure in gneiss slopes of the Xiaowan hydroelectric station, China (Huang et al., 2015). Therefore, it's essential to study the crack evolution behavior of fractured rock in the design and construction of undergound rock tunnels, rock slopes and rock foundations (Li et al., 2016; Liu et al., 2018; Ma et al., 2019a; Zhou et al., 2020a).

During the last decades, many studies have been conducted to explore the rock crack evolution mechanism in the size scale of rock specimens. Pre-exsting flaws are often created in rock or rock-like specimens in laboratory tests in order to clearly observe the crack evolution process (Wong and Einstein, 2009; Yin et al., 2018; Zhang and Zhou, 2020). In this paper, *flaw* refers to the artificial fracture in rock specimens, and *crack* refers to the new fracture under loading. Rectangular prismatic rock or rock-like specimens with relatively small thickness have been extensivly tested in literatures (Zhang et al., 2015; Lin et al., 2019; Zhang et al., 2019), and cracks are always simplified as two-dimensional (2D) ones. However, they are not suitable in complex stress conditions (e.g., unloading of confining pressure) due to limitations of rock mechanics testing system. Therefore, cylindrical rock specimens with pre-existing flaws have been used by a great number of researchers and the number of relevant studies is increasing. At early stage, flaws were cut from the edge to the center of the rock specimen by a sawcut. This kind of artificial flaw is often called edge flaw. Yang et al. (2008) studied marble specimens with two pre-existing edge flaws under various confining pressures. The results indicated that the arrangment of pre-existing flaws affected the peak strength, cohesion and internal friction angle, as well as failure patterns of specimens. Taking granite specimens with

*Corresponding author:
Guo-Qing Chen
State Key Laboratory of Geohazard Prevention and Geoenvironment Protection, Chengdu University of Technology, No. 1 Dongsan Road, Chenghua District, Chengdu 610059, China
Tel: +86-15881086510, E-mail: chgq1982@126.com

one or two pre-existing edge flaws as research objectes, Yao et al. (2019) carried out triaxial compression tests and concluded that post-peak deformation characteristics and failure patterns were determined by configuration of pre-existing flaws and confining pressure. Similar studies on cylindrical rock specimens with pre-existing edge flaws could be found in Wu et al. (2018a) and Zheng et al. (2020). Flaws can be prefabricated in the middle of specimens by using high pressure water jet or wire cutting. This kind of artificial flaw is regarded as central flaw. Lu et al. (2014) investigated the failure process of sandstone specimens with a single central flaw under uniaxial compression. Two kinds of wing cracks, one tensile crack and one anti-tensile crack were identified based on final failure results of their experiment. Huang and Yang (2019) studied granite specimens with two coplanar central flaws by conducting conventional triaxial compression experiment under various confining pressures. In the experiment, noncoalescence, two types of indirect coalescence and one type of shear coalescence were observed as the flaw angle increased from 30° to 60° and the confining pressure increased from 0 to 30 MPa. It is noteworthy that the crack propagation in cylindrical rock specimens was in a 3D manner, which was more complex than that in a 2D manner. However, it is extremely hard to detect 3D crack characteristics in laboratory in opaque rock without using the advanced measurement methods, such as X-ray CT scanning (Kou et al., 2019a), spatial acoustic emission (Eyvind et al., 2014; Shi et al., 2018) and microseismic moment tensor analysis (Li and Einstein, 2019), or special rock-like materials, such as PMMA (Germanovich et al., 1994), transparent materials (Wang et al., 2020) and 3D printing materials (Zhou and Zhu, 2018). It could be found out that strict requrements of techniques and high cost of materials are limations for 3D crack analysis in laboratory experiment.

To better understand the rock fracture coalescence mechanism, numerical simulations have been conducted on rock specimens with pre-existing flaws to provide useful information (e.g., stress field) that is hard to obtain through experiments. Moreover, they could overcome the high cost and time consuming of laboratory experiments. To date, lots of numerical software have been put forward to simulate the rock crack evolution, and have been extended to 3D code, such as RFPA3D (Liang et al., 2012), XFEM (Dehghan et al., 2017), FDEM (Zhou et al., 2020b), EPCA3D (Pan et al., 2009), 3PDEM (Li et al., 2017), EPM (Zhang et al., 2016), PD (Wang et al., 2019) and FLAC3D (Li et al., 2015; Yang et al., 2019). Different numerical methods have their advantages. Priori assumptions about positions and reasons of crack generation are not necessary in RFPA3D. Wang et al. (2014) modeled the crack coalescence behavior of marble speciems with two edge flaws subjected to different confining pressures by using RFPA3D. The results showed that 3D numerical simulation had sound reproduction in the fracture pattern of rock specimens. Bi et al. (2016) simulated the crack evolution mode of 3D penetrating and embedded flaws under biaxial compression in GPD3D. The types of simulated crack coalescence and failure patterns were in line with those of pre-flawed sanstone specimens. Yang et al. (2016) developed 3D NMM to analyze the initiation and propagation of multiple fractures, tensile and shear fractures of rock materials. 3D crack propagation was effective, because 3D code avoided the difficulties of remeshing. Shou et al. (2019) proposed an extended non-ordinary state-based peridynamics to study the propagation and coalescence of 3D flaws of rock specimens. The numerical results were verified by comparing with the simulated results and experimental results. Huang et al. (2019) compared cross sections of fracture by PFC3D simulation and X-ray CT scanning on a sandstone specimen with two edge flaws under conventional triaxial compression. The comparison between numerical and experimental results indicated that numerical simulation could overcome the limitations of visual observation and reveal the distribution of internal cracks. 3D crack behaviors of rock specimens with pre-existing flaws after ultimate failure have been extensively studied by numerical simulation. However, studies about numerical modelling, 3D crack evolution processes of rock specimens with pre-existing flaws are still rare during the whole deformation.

In this study, a laboratory experiment and PFC3D numerical simulation of uniaxial compression were carried out on a cylindrical sandstone specimen with two pre-existing central flaws to explore 3D crack evolution characteristics under loading. In laboratory test, the crack initiation, propagation and coalescence process of sandstone specimens were investigated by photographic and AE monitoring. Additionally, mechanical parameters and failure patterns of two-flawed specimens were reproduced by PFC3D modelling. Finally, the spatial evolution characteristics of fracture patterns were revealed in the numerical simulation.

2. EXPERIMENTAL METHODOLOGY AND RESULTS

2.1. Specimen Preparation

Sandstones used in this experiment were from Rizhao City of Shandong Province, China. They are relatively homogenous without visible beddings and defects. They are dark red and have a bulk density of 2430 kg/m^3. According to the scanning electron microscopy (SEM) result, mineral grains bonded together irregularly with existing micro pores and cracks. The mineral compositions are quartz (9.2%), albite (28.1%), orthoclase (39.4%), dolomite (7.7%), calcite (10.1%) and others (5.5%). The average uniaxial compressive strength is 65.59 MPa, elastic modulus is 11.85 GPa obtained from uniaxial compression, and the tensile strength is 6.67 MPa obtained from Brazilian splitting test.

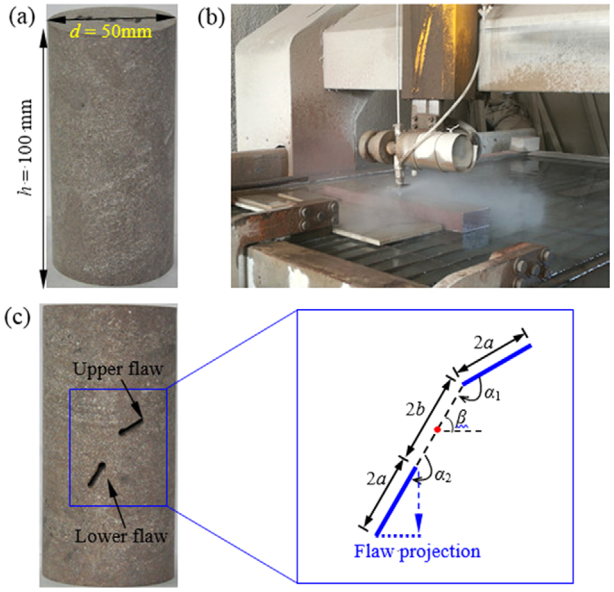

Fig. 1. Geometry of the tested sandstone specimens. (a) Intact specimen. (b) Water jet. (c) Pre-flawed specimen.

Rock cylinders were obtained by coring a large sandstone block along the same direction, and both the top and bottom ends were polished to meet the experimental requirements of ISRM (International Society for Rock Mechanics and Rock Engineering). The specimen's diameter was 50 mm and the height was 100 mm (Fig. 1a). Two straight flaws were cut throughout the sandstone specimen by a high pressure water jet (Fig. 1b). The geometrical parameters of flaws were described as follows. The flaw length 2*a* was 10 mm, the ligament length 2*b* was 11.5 mm, angle between the upper flaw and ligament α_1 was 150°, and angle between the lower flaw and ligament α_1 was 180° (Fig. 1c). Therefore, the upper flaw was unparallel to the ligament, and the lower flaw was parallel to the ligament. In this experiment, the ligament angle β was varied from 60° to 150° at intervals of 30°, while the other geometrical parameters were maintained. Table 1 lists geometrical parameters of sandstone specimens which were tested under different conditions.

2.2. Testing System

The testing system includes a loading system, an AE monitoring and an image acquisition system. A rock mechanics testing system (model SANS-300) with the maximum axial force of 300 kN, was applied in uniaxial compression test. The axial force was applied on the sandstone specimen under displacement-controlled mode with a loading rate of 0.10 mm/min. The force and displacement were recorded automatically during the loading. The external stress was stopped until the failure of sandstone specimen. Real-time monitoring of acoustic signal was realized by AE measurement system (model DS2). One AE sensor was attached to the back of the sandstone specimen, avoiding the influence of image capture of front of the specimen. The fracture process was recorded by a high-definition camera.

2.3. Experimental Results

Figure 2 shows the axial stress-strain curves of sandstone specimens with two pre-existing flaws under uniaxial compression. Two repeated specimens with each ligament angle demonstrated similar performance under the same testing condition (refer to Figs. 2a–e), which was a result of collecting all the specimens from one sandstone block. The pre-peak axial stress-strain curves of the intact and pre-flawed sandstone specimens underwent four stages: crack closure, linear elastic deformation, stable crack propagation and unstable crack propagation (Cai et al., 2004; Nicksiar and Martin, 2012). Sometimes the axial stress falls abruptly and then quickly increases or decreases in the pre-peak curve, which is called a stress drop (Li et al., 2020). Each stress drops generally corresponded to crack initiation, propagation and coalescence manner, which would be investigated in Figure 3. The post-peak curves of the specimens with various ligament angles exhibited sudden drops, due to the brittle behavior of sandstones. The strain at failure of the intact specimen was the highest, and those of pre-flawed specimens varied with the ligament inclination (see Fig. 2f), indicating that the deformation of two-flawed specimens was affected by the ligament inclination.

Table 2 lists the mechanical parameters of sandstone specimens with two pre-existing flaws. Compared to the intact specimens, both the peak strength and elastic modulus of pre-flawed sandstone specimens were lower due to the initial damage of pre-existing flaws. The peak strength first increased and then decreased with the increase of ligament angle. It increased from 29.85 MPa at β = 60° to 47.87 MPa at β = 90° by a 60.3% increment. When β increased from 90° to 150°, it reduced from 47.87 MPa to 32.88

Table 1. Geometry of sandstone specimens with two pre-existing flaws

Specimen number	2*a* (mm)	2*b* (mm)	α_1 (°)	α_2 (°)	β (°)	Type
H1#, H2#	N/A	N/A	N/A	N/A	N/A	Intact specimen
H3#, H4#	10	11.5	150	180	60	Flawed specimen
H5#, H6#	10	11.5	150	180	90	Flawed specimen
H7#, H8#	10	11.5	150	180	120	Flawed specimen
H9#, H10#	10	11.5	150	180	150	Flawed specimen

https://doi.org/10.1007/s12303-021-0013-7

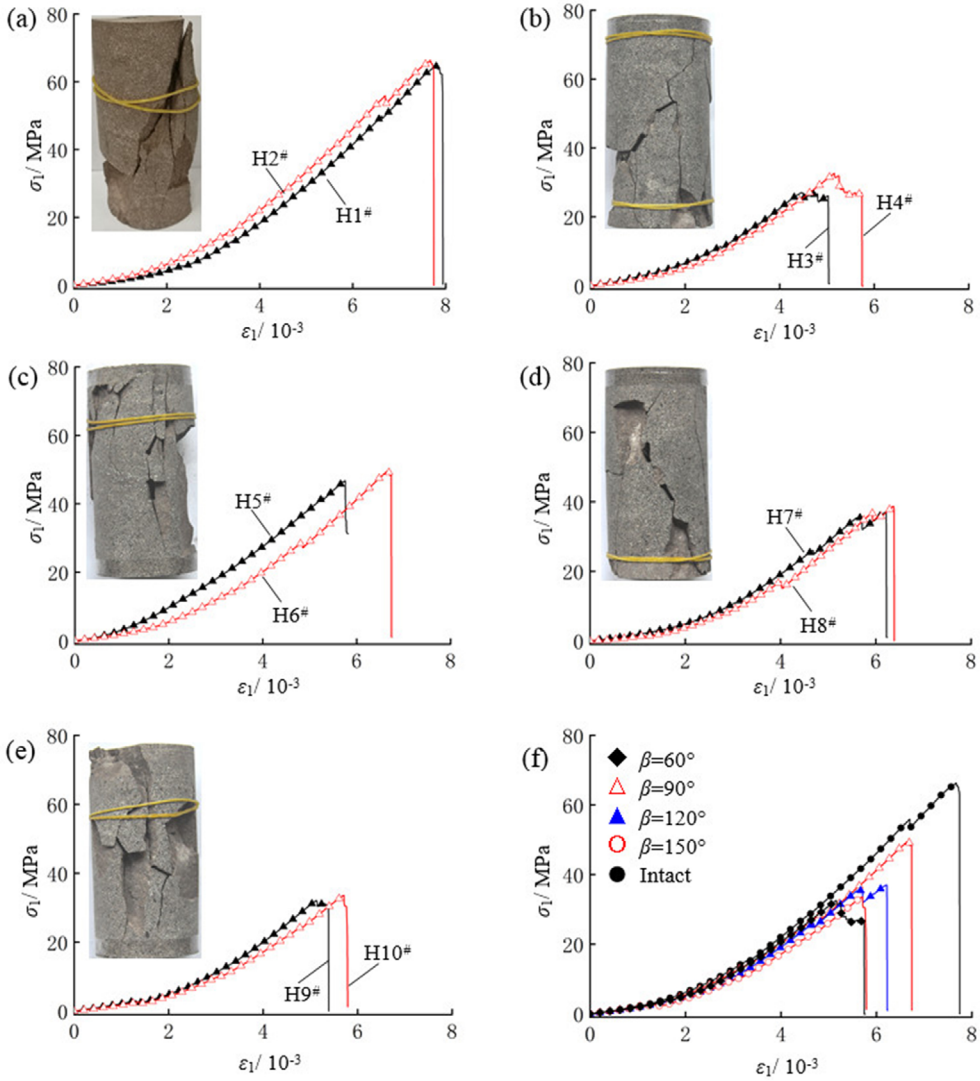

Fig. 2. Test results of sandstone specimens with two pre-existing flaws. (a) Intact specimen. (b) β = 60°. (c) β = 90°. (d) β = 120°. (e) β = 150. (f) Effect of ligament angle.

Table 2. Mechanical parameters of sandstone specimens with two pre-existing flaws

Specimen number	σ_{1c} (MPa)	E_S (GPa)	β (°)
H1#	64.90	11.87	
H2#	66.27	11.82	N/A
Average	65.59	11.85	
H3#	27.11	7.80	
H4#	32.59	9.01	60
Average	29.85	8.40	
H5#	46.72	9.55	
H6#	49.02	9.51	90
Average	47.87	9.53	
H7#	37.04	9.44	
H8#	38.79	8.87	120
Average	37.91	9.16	
H9#	32.15	8.85	
H10#	33.62	8.51	150
Average	32.88	8.68	

MPa by a reduction of 31.3%. The elastic modulus showed a similar trend with the peak strength. It increased to 13.4% when β = 90°, which was higher than that when β = 60°. Afterwards, it decreased from 9.53 GPa to 8.68 GPa with the continuous increasing ligament angle.

From the ultimate failure modes as shown in Figure 2, cracks were generally initiated from the tips of pre-existing flaws. Cracks that initiated from the outer tips of the pre-existing flaws propagated towards the end of the specimen, while cracks that initiated from the inner tips propagated towards the other flaw. Crack coalescence occurred in each specimen when the ligament angle increased from 60° to 150°. The linkage between cracks and flaws formed a macro fracture along the specimen, which caused the coming failure. Far-field cracks and spalling were also observed during the post-peak brittle failure.

Based on previous experimental studies on intact rock specimens

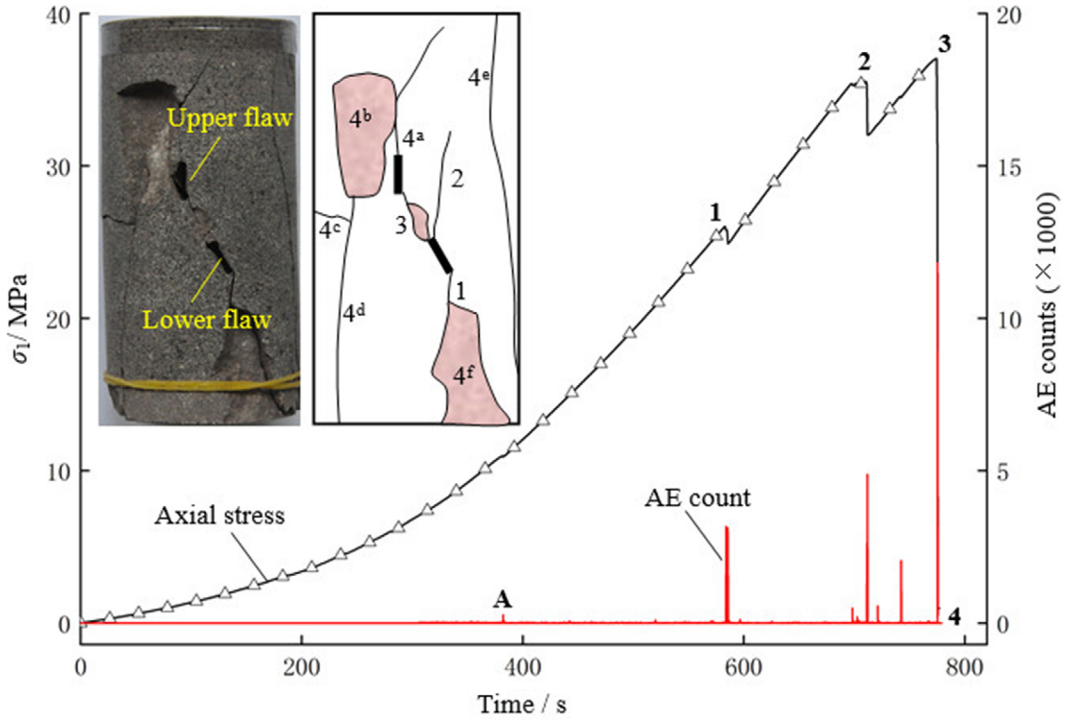

Fig. 3. Crack process and AE counts of sandstone specimen with two pre-existing flaws (β = 120°).

without pre-exiting flaws, AE characteristics could be easily affected by internal damage of rock specimens under loading (Chen et al., 2019; Ma et al., 2019b), and critical stresses can be identified from the accumulated AE curves (Ganne et al., 2007). In order to explore the relationship between AE characteristics and crack evolution process in pre-flawed sandstone specimens, the evolution of AE count and crack process were presented in this paper. The pre-flawed sandstone specimen (β = 120°) was taken as an example, as shown in Figure 3. Many stress drops were observed in the axial stress curve, indicating that the fracture of sandstone specimens with pre-existing flaws was a progressive process. The first visible stress drop occurred when the axial stress increased to 26.05 MPa. Crack 1 was initiated from the outer tip of the lower flaw (i.e., inclined flaw), leading to an obvious AE count. Crack 2 was initiated from the inner tip of the lower flaw, resulting in a sudden drop in axial stress and an abrupt increment in AE count, when the specimen was loaded to Point 2 (σ_1 = 35.30 MPa). When the axial stress dropped to 32.02 MPa, it continued to increase and reached the peak. At that moment, crack coalescence occurred due to the propagation of Crack 3. No cracks were initiated from the outer tip of the upper flaw (i.e., vertical flaw) before the peak strength. Due to the brittle characteristics of the tested sandstone, the specimen failed abruptly after the occurrence of crack coalescence. Cracks 4^{a-f} were formed during the failure. However, all the above-mentioned cracks were observed from the front surface of the specimen. It is noteworthy that each stress drop corresponded to a sudden increment in AE count curve, but the converse might be not true. It was mainly because the stress drop was induced by crack acceleration to critical value, while AE increase was a sign of the enhancement of local crack. More specifically, a crack might be initiated in the inner or back surface of the specimen when the sudden increment of AE occurred, which was not detected on the front surface of the specimen. When the specimen was loaded to Point A, a low increment in AE count was observed, which was significantly lower than that at Points 1–4, because the first crack had not been completely formed at that moment.

3. NUMERICAL SIMULATION AND ERSULTS

PFC has been widely used in modelling fracture behaviors of rock specimens under various loading conditions (Yang and Qiao, 2018; Kou et al., 2019b; Cheng and Wong, 2020). It performs well in the reproduction of crack process and analysis of meso-mechanism of rock fracture. Therefore, PFC3D was used to reveal 3D crack behaviors of cylindrical sandstone specimens in this section.

3.1. Numerical Model

From the surface image of the tested sandstone under optical microscopy, grains were bonded tightly by cementation as shown in Figure 4a. To simulate the microscopic structure of the sandstone, parallel-bond model (PBM) in PFC3D was used to build the

https://doi.org/10.1007/s12303-021-0013-7

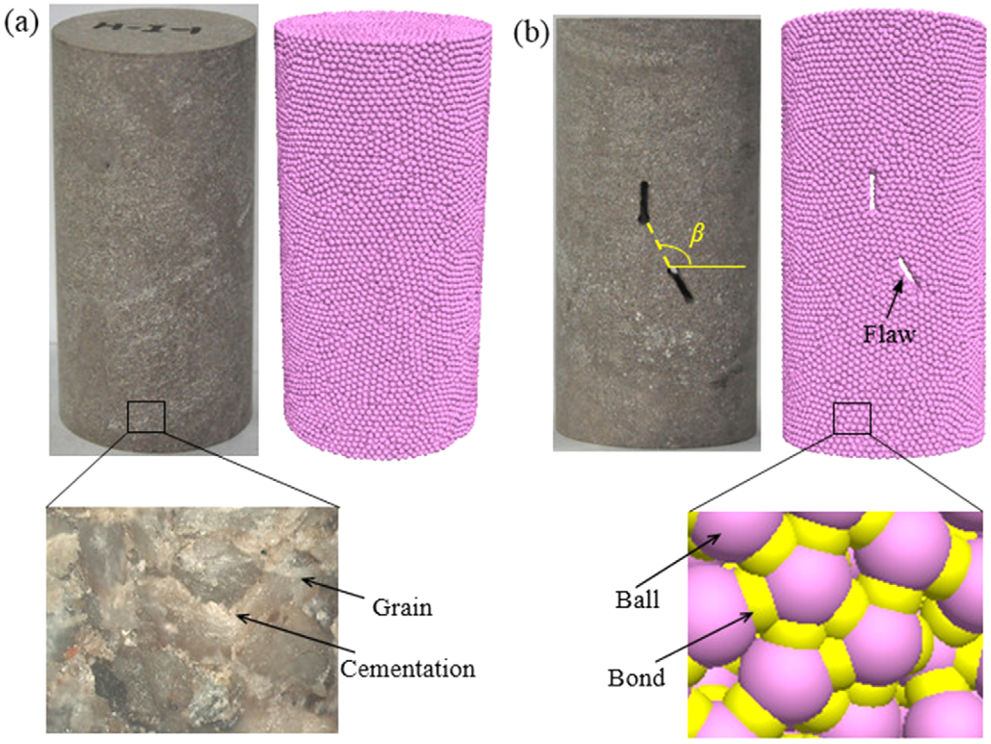

Fig. 4. Numerical models of the intact sandstone specimen and the pre-flawed specimen. (a) Intact specimen. (b) Pre-flawed specimen.

numerical specimen. The specimen has the diameter of 50 mm and height of 100 mm, which is the same as the sandstone specimen in the laboratory test. Two open flaws were created in the center of the specimen. Two pre-existing flaws in PFC3D were copied from the laboratory experiment (Fig. 4b). The ligament angle β varied from 60° to 150° at intervals of 30°.

3.2. Parameter Calibration

Before the numerical simulation of pre-flawed specimens, micro parameters that determine the mechanical behavior of the specimens should be calibrated. Based on previous studies (Cao et al., 2016; Wu et al., 2018b), micro parameters of PBM were calibrated by comparing the numerical and experimental results of intact specimens. Table 3 shows the calibrated micro-parameters.

Figure 5 shows the comparison results between numerical simulation and experiment of intact sandstone specimens. The numerical stress-strain curve couldn't match well with that in the experiment at the initial compaction stage, because the current PBM couldn't simulate the initial crack closure. However, the slope and peak of the numerical stress-strain curve were in consistent with the experimental results. At this point, shear fracture was dominated in the failure of the intact sandstone specimen under uniaxial compression. The numerical specimen also failed with shear mode, indicating that the numerical failure mode was in line with that in the experiment. Finally, the calibrated micro parameters listed in Table 3 were used in the simulation of pre-flawed specimens.

Table 3. Micro parameters in PFC3D

Micro-parameters	Values
Density of the ball (kg/m^3)	2430
Contact modulus of the ball (GPa)	9.5
Contact modulus of the parallel bond (GPa)	9.5
Ratio of normal to shear stiffness of the ball	1.8
Ratio of normal to shear stiffness of the parallel bond	1.8
Ball friction coefficient	0.35
Parallel-bond normal strength, mean (MPa)	32
Parallel-bond normal strength, standard deviation (MPa)	7
Parallel-bond shear strength, mean (MPa)	45
Parallel-bond shear strength, standard deviation (MPa)	9

3.3. Numerical Results

Figure 6 shows axial stress-strain curves of numerical specimens with two pre-existing flaws under uniaxial compression. It also gives the number of microcracks curves of flawed specimens. A microcrack formed when a parallel bond between adjacent particles was broken (Potyondy and Cundall, 2004), which is represented as a blue facet in this simulation. The simulated stress-strain curves of flawed specimens were similar to those in the experiment. However, stress drops in the pre-peak curves

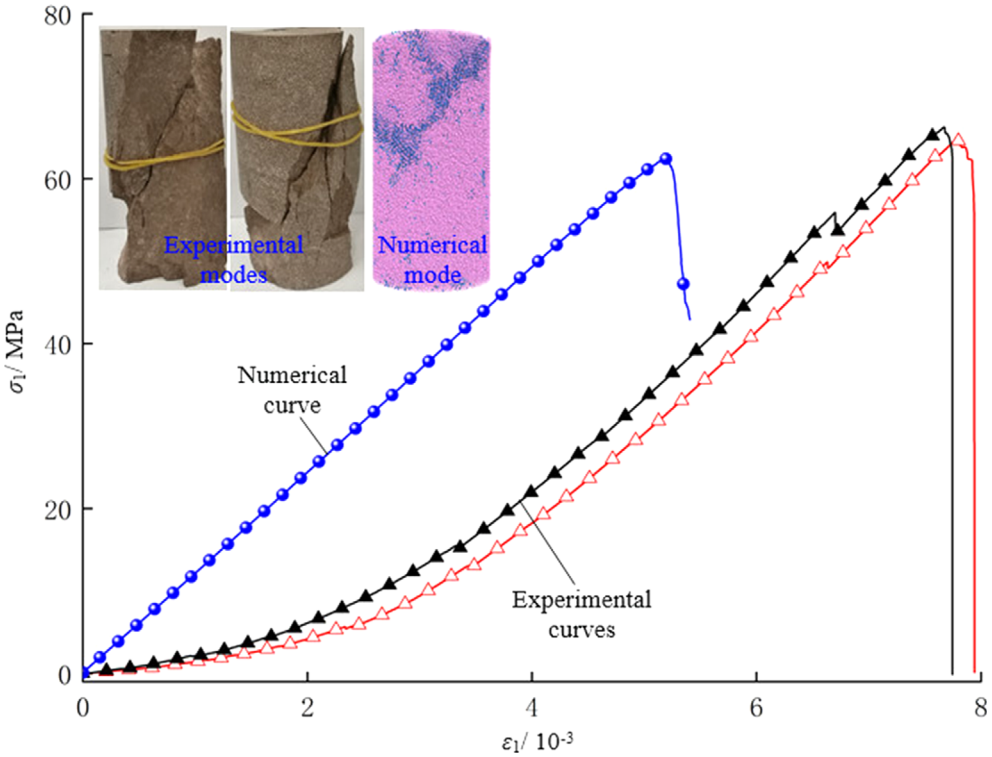

Fig. 5. Comparison between numerical and experimental results of intact sandstone specimens.

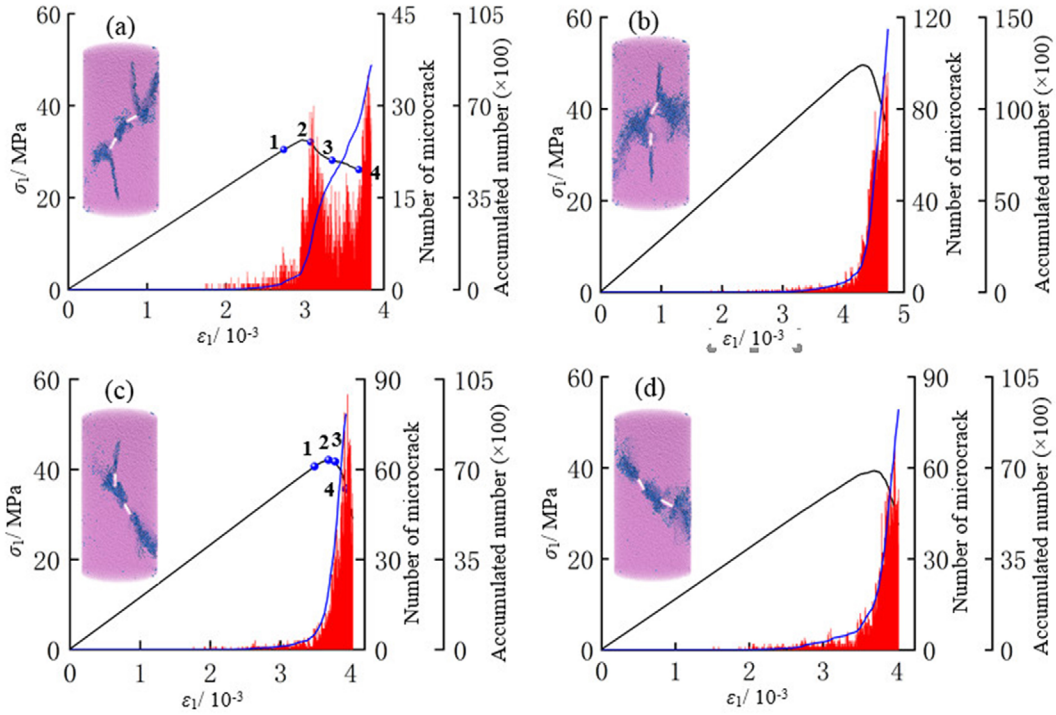

Fig. 6. Stress-strain and number of microcrack curves of numerical two-flawed specimens. (a) β = 60°. (b) β = 90°. (c) β = 120°. (d) β = 150°.

were not reproduced in the numerical simulation. At the initial loading stage, microcracks were not active and few microcracks were observed. They started to initiate rarely when the axial stress increased before the peak strength. They became active near the peak strength. Thus, the accumulated microcrack curves increased slowly before the peak strength, followed by sharp increases after the peak strength.

The fracture patterns of numerical pre-flawed specimens at

https://doi.org/10.1007/s12303-021-0013-7

the front surface consisted with those in the experiment (Fig. 2), in particular those around the pre-existing flaws. Differences between numerical simulation and experiment were observed in the fractures far away from the pre-existing flaws. Surface spalling 4^{b} and tensile cracks 4^{c-e} generated during the abrupt failure of brittle sandstone specimen (refer to Fig. 3) were not observed. It indicates that rock brittle characteristics cannot be fully reproduced in the numerical simulation. Crack patterns at the front and back surface were not always the same. Thus, it is necessary to study the internal 3D fracture process of pre-flawed specimens during loading.

To reveal spatial characteristics of fracture, the internal crack evolution process during the compressive loading was obtained by the numerical simulation. The crack initiation, propagation and coalescence processes of the pre-flawed specimen with β = 60° are shown from the front view and left view in Figure 7. The front view shows that as the axial stress increased, microcracks were concentrated around four tips of the pre-existing flaws. When it increased to 31.85 MPa (Point 1) before the peak strength, macrocracks that composed of several microcracks were observed from each tip of the pre-existing flaws. After the peak strength, microcracks became active. In the range of peak stress to Point 2, most of the new microcracks were initiated in the ligament region. It resulted in crack coalescence between the inner tips of flaws when the numerical specimen was loaded to Point 2 (σ_1 = 32.13MPa) after the peak strength. At the moment, wing cracks from the outer tip of the upper flaw propagated upwards along z-axis direction, while those from the outer tip of the lower flaw propagated downwards. With the increase of microcracks, wing cracks lengthened. They were parallel to the loading direction when the axial stress reached Point 3 (σ_1 = 28.16 MPa). During the growth of wing cracks, some microcracks were initiated near the outer tips and parallel to the flaw direction. When the numerical specimen was loaded to Point 4 (σ_1 = 26.11 MPa), two coplanar secondary cracks were observed from two outer tips of flaws. From the left viewpoint, when the specimen was loaded to Point 1, microcracks were irregularly distributed at the tips of flaws along y-axis direction of the specimen thickness.

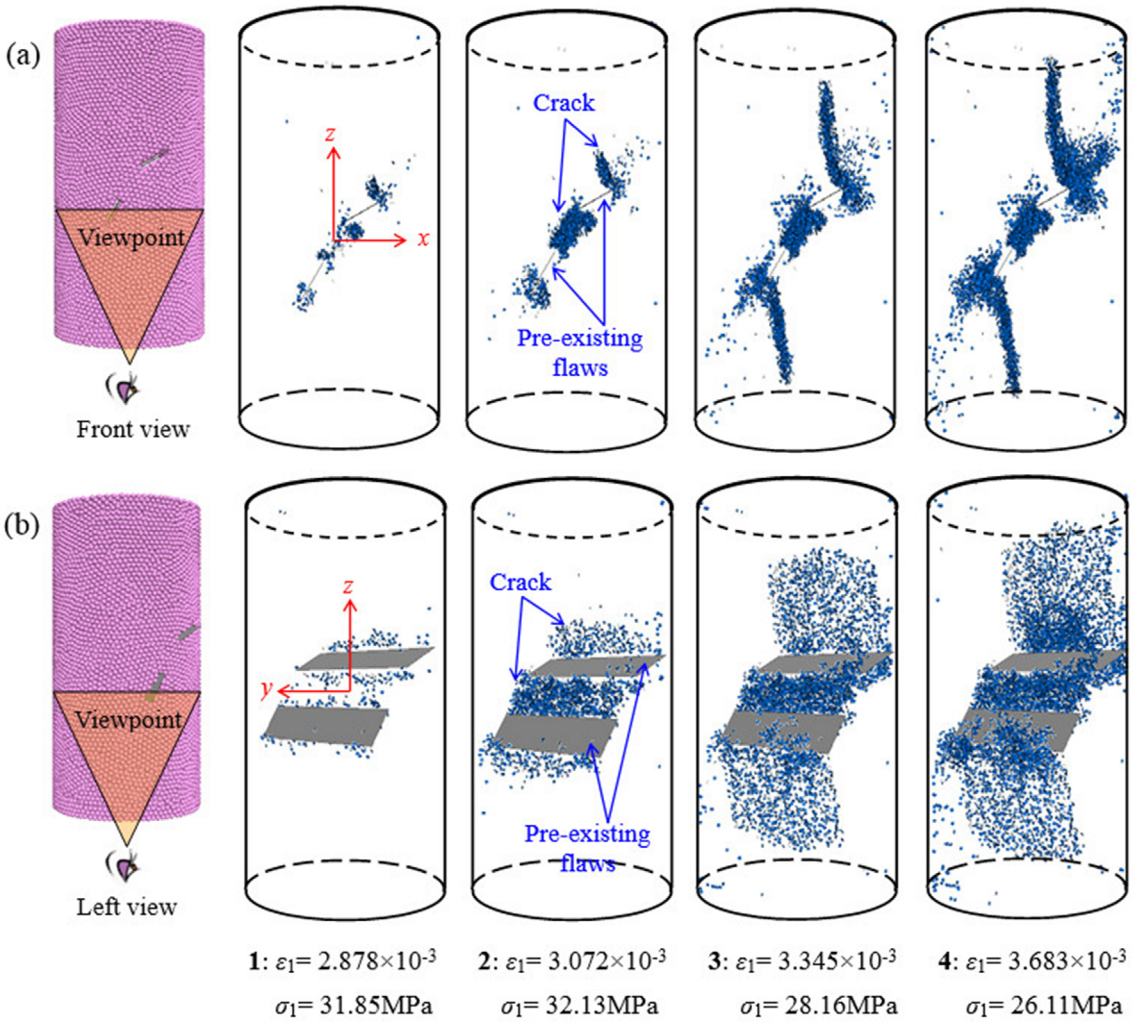

Fig. 7. Spatial cracking process of numerical pre-flawed specimen (β = 60°). (a) Fracturing from front viewpoint. (b) Fracturing from left viewpoint.

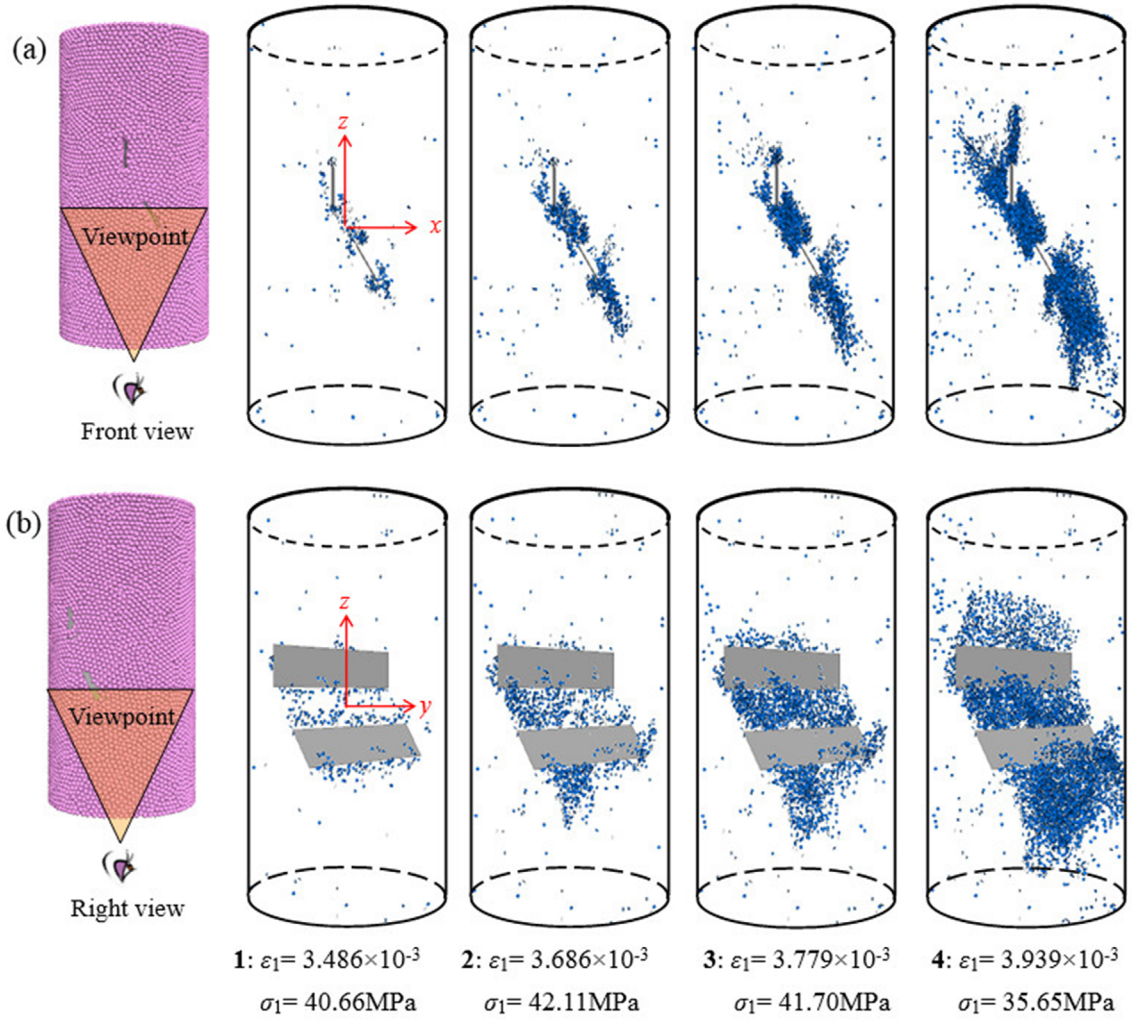

Fig. 8. Spatial cracking process of numerical pre-flawed specimen (β = 120°). (a) Fracturing from front viewpoint. (b) Fracturing from right viewpoint.

When the axial stress increased to Point 2, microcracks in the ligament region acted as a rough surface and coalesced inner tips of two flaws. When the specimen was loaded to Point 3, two wing cracks from outer tips of flaws looked like a curved surface. Crack pattern at Point 4 was symmetrical along y-axis direction.

Figure 8 shows the internal crack initiation, propagation and coalescence processes of pre-flawed specimen with β = 120° from the front view and right view. Similar to the above specimen with β = 60°, microcracks were also initiated from pre-existing flaw tips of pre-flawed specimen with β = 120°. When the axial stress increased to Point 1 (σ_1 = 40.66 MPa), some microcracks were observed from the tips of flaws, except for the outer tip of the upper flaw. Cracks from the outer tip of the lower flaw propagated parallel to the flaw, and crack coalescence occurred between two inner tips of flaws, when the axial stress reached the peak (Point 2). Only few microcracks were seen from the outer tip of the upper flaw at that moment. A crack, which was coplanar to the coalesced crack, was initiated from the inner tip of the upper flaw and propagated upwards. It is seen that the tensile crack from the outer tip of the upper flaw started to form at Point 3 (σ_1 = 41.70 MPa) at the post-peak stage. With the continuous loading, the number of microcracks became more and more, and thus macrocracks lengthened and widened. The upward tensile crack from the outer tip of the upper flaw was longer than the pre-existing flaw when the specimen was loaded to Point 4 (σ_1 = 35.65 MPa). Figure 8b demonstrates that cracks in the pre-flawed specimen with β = 120° were not symmetrical along y-axis direction. Cracks initiated from the outer tip of the lower flaw were observed. At the beginning, microcracks were initiated randomly along the thickness direction of the specimen when the specimen was loaded to Point 1. However, more microcracks were observed in the front side than the back side of numerical specimen, which was mainly due to the heterogeneity of the numerical specimen. At Points 2, 3 and 4, macrocracks from

https://doi.org/10.1007/s12303-021-0013-7

the outer tip of the lower flaw were longer in the front side than the back side of numerical specimen. The crack characteristics indicated that the fracture distribution at the front and back surface was not always identical, which was consistent with the experimental result of multiple-holed granite specimens (Wong and Lin, 2015).

To further detect the internal fracture, the 3D crack distribution was plotted at ultimate failure from the left view (β = 60° and 90°) and right view (β = 120° and 150°) in Figure 9. In general, the closer to the pre-existing flaws, the denser of the microcracks were (Fig. 9a). In accordance with the internal crack distribution of the pre-flawed specimen, a sketch of two crack coalescence modes between two pre-existing flaws was plotted based on the simulated results (Fig. 9b). One was the direct coalescence by one crack connecting two inner tips of flaws (β = 60°, 120° and 150°). The other was the indirect coalescence by two cracks linked with two inner tips of flaws (β = 90°). The internal fracture photographs of sandstone specimens were captured through poking sandstone specimens after their failure (Fig. 9c). The failure patterns obtained from experimental results were similar with those in the numerical simulation. These fracture images further indicated that fracture distributions were not always identical at the front and back surfaces. On the other hand, these fracture images are useful to distinguish the classification of cracks. When the ligament angle was 60°, the fracture surfaces of wing cracks initiated from the outer tips of pre-existing flaws were rough and no friction traces were observed. However, the fracture surfaces of coalesced cracks were rough with obvious friction traces. It could be inferred that the wing crack was a tensile crack, while the coalesced crack was a mix of tensile and shear crack.

4. DISCUSSION

Figure 10a shows the comparison of peak strength of two-

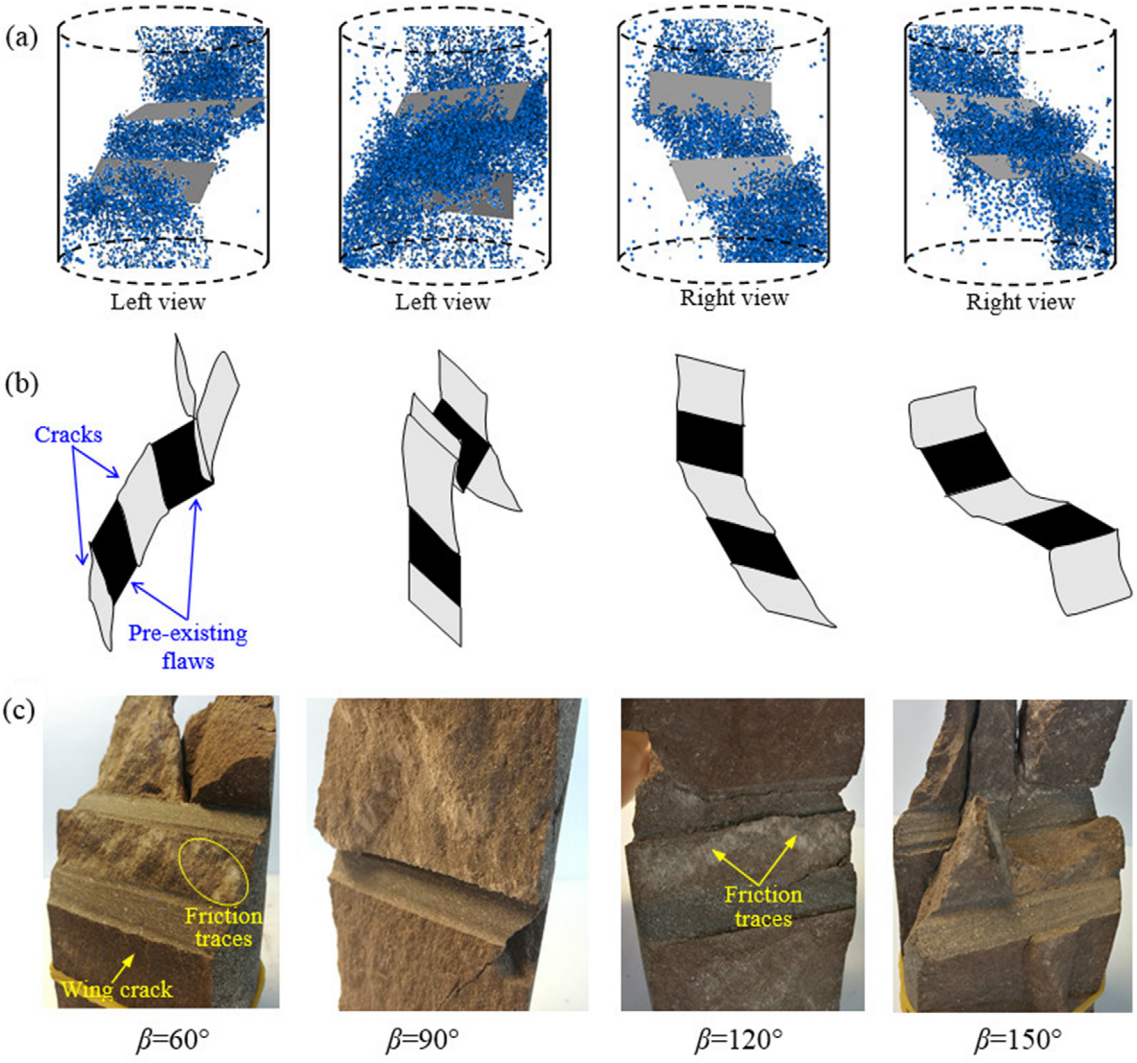

Fig. 9. Typical failure modes of sandstone specimens containing two pre-existing flaws. (a) Simulated results. (b) Sketch of crack coalescence mode. (c) Experimental results.

flawed specimens between numerical simulation and laboratory experiment. There was a minor difference in values and the variation trends of peak strength with the increase of ligament angle were the same. The peak strength first increased and then decreased when the ligament angle β increased from 60° to 150°. In the numerical simulation, crack initiation stress referred to the axial stress when the number of microcracks reached 10% of that at the peak strength. The evolution of simulated crack initiation stress was similar to that of peak strength. With the increase of the ligament angle, the crack initiation stress first increased and then decreased, reaching the maximum value when β = 90°.

To reveal the variation of crack initiation stress, force distribution around two pre-existing flaws was obtained in the numerical modelling. Figure 10b shows the force distribution with different ligament angle when the axial stress is applied to 5 MPa before the first crack initiation. Blue color and green color stand for

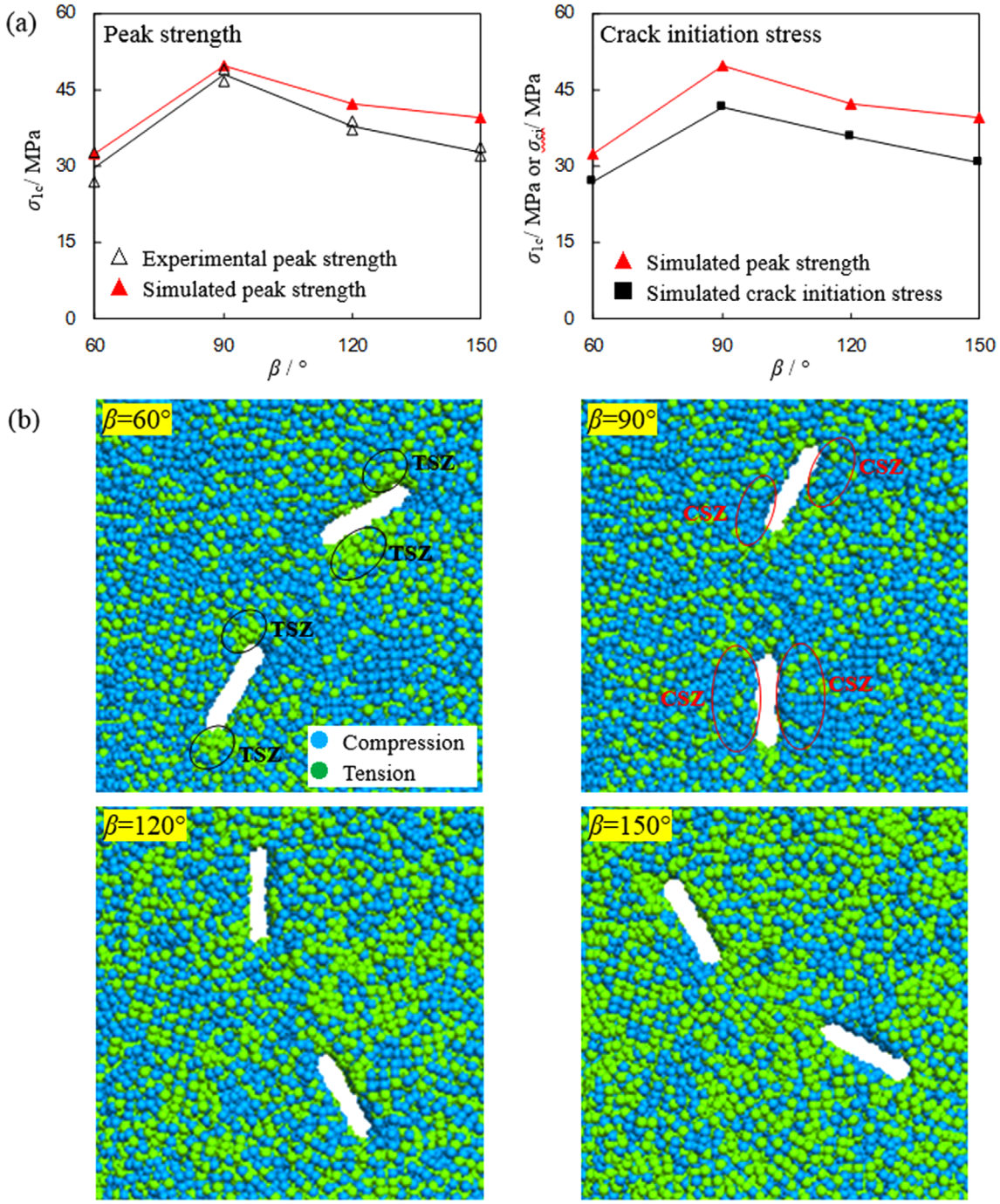

Fig. 10. Strength of pre-flawed specimen and force distribution around the pre-existing flaw. (a) Peak strength and crack initiation stress. (b) Force distribution around the pre-existing flaw.

https://doi.org/10.1007/s12303-021-0013-7

compressive force and tensile force, respectively. "TSZ" means tensile stress concentration zone, and "CSZ" means compressive stress concentration zone. When the ligament angle was 60°, tensile stress concentration was clearly at the tips of pre-existing flaws, whose position was consistent with the crack initiation in Figure 6. When the ligament angle increased to 90°, most parts of the pre-existing flaws were crowded by the compressive stress, and tensile stress concentration was observed at two lower tips of the flaws, whose area was narrower, compared to the specimen with $\beta = 60°$. It could be inferred that cracks were more difficult to initiate in the specimen with $\beta = 90°$ than that with $\beta = 60°$. Therefore, the crack initiation stress increased when the ligament angle increased from 60° to 90°. When the ligament angles were 120° and 150°, tensile stress concentration was observed around the flaws, and the area with $\beta = 150°$ was larger than that with $\beta = 120°$. Therefore, the crack initiation stress decreased when the ligament angle increased from 90° to 150°.

However, the above-mentioned experimental and simulated results with respect to ligament angle were based on the specific flaw geometrical parameters when the lower flaw was parallel to the ligament (i.e., $\alpha_2 = 180°$). To further investigate the effects of ligament parameters on the strength and deformability of rock, more simulation on pre-flawed specimens was carried out when the lower flaw was unparallel to the ligament (i.e., $\alpha_2 = 210°$ and 240°). Figure 11 shows the effects of ligament angle and ligament length on the mechanical properties of pre-flawed specimens. From Figures 11a and b, it is seen that the peak strength and elastic modulus of pre-flawed specimens first increased and then decreased with the increase of ligament angle. However, the ligament angles at which the peak strength and elastic modulus reach their maximum values were different for different angles of α_2. When the angle of α_2 was 180°, the corresponding ligament angle at which the mechanical properties reach their maximum values was 90°. When the angle of α_2 was 210° or 240°, the corresponding ligament angle was 120°. The evolution trend of mechanical properties of pre-flawed specimens can be explained from the projected length of pre-existing flaw in the loading direction (refer to Fig. 1c). When the angle of α_2 was 180°, the vertically-projected length first decreased and then increased, reaching its minimum value at $\beta = 90°$. When the angle of α_2 was 210° or 240°, the vertically-

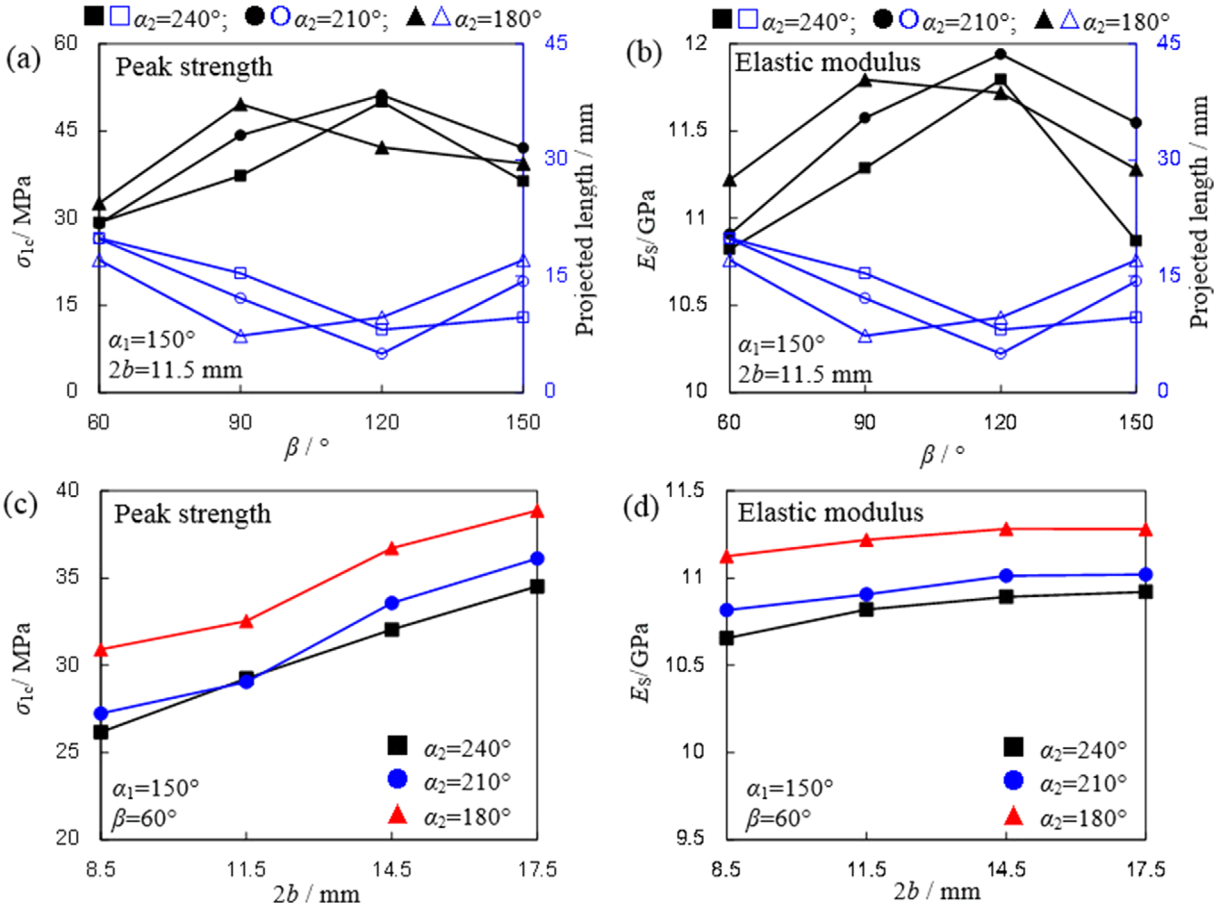

Fig. 11. Effects of ligament angle and ligament length on the mechanical properties of pre-flawed specimens. (a) Effect of ligament angle on peak strength. (b) Effect of ligament angle on elastic modulus. (c) Effect of ligament length on peak strength. (d) Effect of ligament length on elastic modulus.

projected length first decreased and then increased, reaching its minimum value at $\beta = 120°$. Under the arrangement of two-flaws in this simulation, the peak strength and elastic modulus of pre-flawed specimens exhibited negative correlation with the projected length of pre-existing flaw in the loading direction. This finding is similar to the previous studies (Jiang et al., 2015; Zhang et al., 2020). Note that this explain did not consider the variation of stress distribution during the increase of ligament angle. It can be seen from Figures 11c and d that the peak strength and elastic modulus of pre-flawed specimens increased with increasing ligament length, which is might be the decreasing interaction between two pre-existing with lengthening ligament. This argument is supported by previous experiment and simulation conducted by Zhang and Wong (2012) and Du et al. (2020).

Some previous studies have been conducted to investigate the crack coalescence behavior of cylindrical rock specimens containing pre-existing flaws. Compared with these previous studies (Wu et al., 2018b; Yang et al., 2018; Yao et al., 2018; Huang et al., 2019), pre-existing flaws were cut in the center of specimen in this experiment and simulation. One of advantages of rock specimens with central flaws is that it could minimize boundary effects on rock cracking behaviors. Furthermore, internal spatial crack initiation, propagation and coalescence process was analyzed during the loading, which is not obtained in these previous studies. With the analysis of internal cracking process, the understanding of 3D crack mechanism of rock is enhanced.

5. CONCLUSIONS

(1) As the ligament angle increased from 60° to 150°, the peak strength and elastic modulus of sandstone specimens that contain two pre-existing flaws first increased and then decreased, which exhibited negative correlation with the projected length of pre-existing flaw in the loading direction. The ligament angles at which the mechanical properties reach their maximum values were different for different flaw angles. Moreover, the peak strength and elastic modulus of pre-flawed specimens increased with increasing ligament length.

(2) The internal crack evolution process during the loading was investigated by the numerical simulation. Microcracks that initiate from the tips of pre-existing flaws due to the tensile stress concentration formed macrocracks. Macracracks propagated toward tips of pre-flaws in the ligament area, and the ends of specimen outside the ligament area. The crack coalescence between two neighboring tips of pre-flaws divided the specimen into several parts. From the three dimensional viewpoint, the macrocrack acted as a rough curved surface inside the specimen.

(3) The ultimate failure patterns of numerical specimens with two pre-existing flaws agreed with the experimental results. Two types of crack coalescence were identified between the pre-existing flaws. One was the direct coalescence induced by one crack connecting two inner tips of flaws, and the other was the indirect coalescence by two cracks linked with two inner tips of flaws.

ACKNOWLEDGMENTS

This research was supported by the National Natural Science Foundation of China (51909260, 41972284), the China Postdoctoral Science Foundation (2021M693424) and the Opening Fund of State Key Laboratory of Geohazard Prevention and Geoenvironment Protection, Chengdu University of Technology (SKLGP2020K011). The authors would also like to express their sincere gratitude to the editor and anonymous reviewers for their valuable comments, which have greatly improved this paper.

REFERENCES

Bi, J., Zhou, X.P., and Qian, Q.H., 2016, The 3D numerical simulation for the propagation process of multiple pre-existing flaws in rock-like materials subjected to biaxial compressive loads. Rock Mechanics and Rock Engineering, 49, 1611–1627.

Cai, M., Kaiser, P.K., Tasaka, Y., Maejima, T., Morioka, H., and Minami, M., 2004, Generalized crack initiation and crack damage stress thresholds of brittle rock masses near underground excavations. International Journal of Rock Mechanics and Mining Science, 41, 833–847.

Cao, R.H., Cao, P., Lin, H., Pu, C.Z., and Ou, K., 2016, Mechanical behavior of brittle rock-like specimens with pre-existing fissures under uniaxial loading: experimental studies and particle mechanics approach. Rock Mechanics and Rock Engineering, 49, 763–783.

Chen, G., Li, T., Wang, W., Zhu, Z., Chen, Z., and Tang, O., 2019, Weakening effects of the presence of water on the brittleness of hard sandstone. Bulletin of Engineering Geology and the Environment, 78, 1471–1483.

Cheng, Y. and Wong, L.N.Y., 2020, A study on mechanical properties and fracturing behavior of Carrara marble with the flat-jointed model. International Journal for Numerical and Analytical Methods in Geomechanics, 44, 803–822.

Dehghan, A.N., Goshtasbi, K., Ahangari, K., Jin, Y., and Bahmani, A., 2017, 3D numerical modeling of the propagation of hydraulic fracture at its intersection with natural (pre-existing) fracture. Rock Mechanics and Rock Engineering, 50, 367–386.

Du, Y., Li, T., Li, W., Ren, Y., Wang, G., and He, P., 2020, Experimental study of mechanical and permeability behaviors during the failure of sandstone containing two preexisting fissures under triaxial compression. Rock Mechanics and Rock Engineering, 53, 3673–3697.

Eyvind, A., Kühn, D., Vavryčuk, V., Soldal, M., and Oye, V., 2014, Experimental investigation of acoustic emissions and their moment tensors in rock during failure. International Journal of Rock Mechanics and Mining Sciences, 70, 286–295.

https://doi.org/10.1007/s12303-021-0013-7

Ganne, P., Vervoort, A., and Wevers, M., 2007, Quantification of pre-peak brittle damage: correlation between acoustic emission and observed micro-fracturing. International Journal of Rock Mechanics and Mining Sciences, 2007, 44, 720–729.

Germanovich, L.N., Salganik, R.L., Dyskin, A.V., and Lee, K.K., 1994, Mechanics of brittle fracture with pre-existing cracks in compression. Pure and Applied Geophysics, 143, 117–149.

Huang, D., Cen, D., Ma, G., and Huang, R., 2015, Step-path failure of rock slopes with intermittent joints. Landslides, 12, 911–926.

Huang, Y.H. and Yang, S.Q., 2019, Mechanical and cracking behavior of granite containing two coplanar flaws under conventional triaxial compression. International Journal of Damage Mechanics, 28, 590–610.

Huang, Y.H., Yang, S.Q., and Tian, W.L., 2019, Crack coalescence behavior of sandstone specimen containing two pre-existing flaws under different confining pressures. Theoretical and Applied Fracture Mechanics, 99, 118–130.

Jiang, M., Chen, H., and Crosta, G.B., 2015, Numerical modeling of rock mechanical behavior and fracture propagation by a new bond contact model. International Journal of Rock Mechanics and Mining Sciences, 78, 175–189.

Kou, M., Liu, X., Tang, S., and Wang, Y., 2019a, 3-D X-ray computed tomography on failure characteristics of rock-like materials under coupled hydro-mechanical loading. Theoretical and Applied Fracture Mechanics, 104, 102396.

Kou, M.M., Lian, Y.J., and Wang, Y.T., 2019b, Numerical investigations on crack propagation and crack branching in brittle solids under dynamic loading using bond-particle model. Engineering Fracture Mechanics, 212, 41–56.

Li, B.Q. and Einstein, H.H., 2019, Direct and microseismic observations of hydraulic fracturing in Barre granite and Opalinus clayshale. Journal of Geophysical Research: Solid Earth, 124, 11900–11916

Li, C., Hu, Y., Meng, T., Jin, P., Zhao, Z., and Zhang, C., 2020, Experimental study of the influence of temperature and cooling method on mechanical properties of granite: implication for geothermal mining. Energy Science and Engineering, 8, 1716–1728.

Li, X.F., Li, H.B., and Zhao, J., 2017, 3D polycrystalline discrete element method (3PDEM) for simulation of crack initiation and propagation in granular rock. Computers and Geotechnics, 90, 96–112.

Li, Y., Zhou, H., Zhu, W.S., Li, S.C., and Liu, J., 2015, Numerical study on crack propagation in brittle jointed rock mass influenced by fracture water pressure. Materials, 8, 3364–3376.

Li, Y., Zhou, H., Zhu, W.S., Li, S.C., and Liu, J., 2016, Experimental and numerical investigations on the shear behavior of a jointed rock mass. Geosciences Journal, 20, 371–379.

Liang, Z.Z., Xing, H., Wang, S.Y., Williams, D.J., and Tang, C.A., 2012, A three-dimensional numerical investigation of the fracture of rock specimens containing a pre-existing surface flaw. Computers and Geotechnics, 45, 19–33.

Lin, H., Yang, H., Wang, Y., Zhao, Y., and Cao, R., 2019, Determination of the stress field and crack initiation angle of an open flaw tip under uniaxial compression. Theoretical and Applied Fracture Mechanics, 104, 102358.

Liu, Y., Dai, F., Dong, L., Xu, N., and Feng, P., 2018, Experimental investigation on the fatigue mechanical properties of intermittently jointed rock models under cyclic uniaxial compression with different loading parameters. Rock Mechanics and Rock Engineering, 51, 47–68.

Lu, Z.D., Chen, C.X., Feng, X.T., and Zhang, Y.L., 2014, Strength failure and crack coalescence behavior of sandstone containing single precut fissure under coupled stress, fluid flow and changing chemical environment. Journal of Central South University, 21, 1176–1183.

Ma, D., Duan, H., Li, X., Li, Z.H., Zhou, Z.L., and Li, T.B., 2019a, Effects of seepage-induced erosion on nonlinear hydraulic properties of broken red sandstones. Tunnelling and Underground Space Technology, 91, 102993.

Ma, D., Wang, J., Cai, X., Ma, X.T., Zhang, J.X., Zhou, Z.L., and Tao, M., 2019b, Effects of height/diameter ratio on failure and damage properties of granite under coupled bending and splitting deformation. Engineering Fracture Mechanics, 220, 106640.

Nicksiar, M. and Martin, C.D., 2012, Evaluation of methods for determining crack initiation in compression tests on low-porosity rocks. Rock Mechanics and Rock Engineering, 45, 607–617.

Pan, P.Z., Feng, X.T., and Hudson, J.A., 2009, Study of failure and scale effects in rocks under uniaxial compression using 3D cellular automata. International Journal of Rock Mechanics and Mining Sciences, 46, 674–685.

Potyondy, D.O. and Cundall, P.A., 2004, A bonded-particle model for rock. International Journal of Rock Mechanics and Mining Sciences, 41, 1329–1364.

Shi, G., Yang, X., Yu, H., and Zhu, C., 2018, Acoustic emission characteristics of creep fracture evolution in double-fracture fine sandstone under uniaxial compression. Engineering Fracture Mechanics, 210, 13–28.

Shou, Y.D., Zhou, X.P., and Berto, F., 2019, 3D numerical simulation of initiation, propagation and coalescence of cracks using the extended non-ordinary state-based peridynamics. Theoretical and Applied Fracture Mechanics, 101, 254–268.

Wang, H., Dyskin, A., Pasternak, E., Dight, P., and Sarmadivaleh, M., 2020, Experimental and numerical study into 3D crack growth from a spherical pore in biaxial compression. Rock Mechanics and Rock Engineering, 53, 77–102.

Wang, S.Y., Sloan, S.W., Sheng, D.C., Yang, S.Q., and Tang, C.A., 2014, Numerical study of failure behaviour of pre-cracked rock specimens under conventional triaxial compression. International Journal of Solids and Structures, 51, 1132–1148.

Wang, Y.T., Zhou, X.P., and Kou, M.M., 2019, Three-dimensional numerical study on the failure characteristics of intermittent fissures under compressive-shear loads. Acta Geotechnica, 14, 1161–1193.

Wong, L.N.Y. and Einstein, H.H., 2009, Crack coalescence in molded gypsum and Carrara marble: Part 1. macroscopic observations and interpretation. Rock Mechanics and Rock Engineering, 42, 475–511.

Wong, R.H.C. and Lin, P., 2015, Numerical study of stress distribution and crack coalescence mechanisms of a solid containing multiple holes. International Journal of Rock Mechanics and Mining Sciences, 79, 41–54.

Wu, J., Feng, M., Mao, X., Xu, J., Zhang, W., Ni, X., and Han, G., 2018a, Particle size distribution of aggregate effects on mechanical and structural properties of cemented rockfill: experiments and modeling. Construction and Building Materials, 193, 295–311.

Wu, J., Feng, M., Yu, B., and Han, G., 2018b, The length of pre-existing fissures effects on the mechanical properties of cracked red sandstone and strength design in engineering. Ultrasonics, 82, 188–199.

Yang, S.Q., Huang, Y.H., and Ranjith, P.G., 2018, Failure mechanical and acoustic behavior of brine saturated-sandstone containing two pre-existing flaws under different confining pressures. Engineering Fracture Mechanics, 193, 108–121.

Yang, S.Q., Jiang, Y.Z., Xu, W.Y., and Chen, X.Q., 2008, Experimental investigation on strength and failure behavior of pre-cracked marble under conventional triaxial compression. International Journal of Solids and Structures, 45, 4796–4819.

Yang, W., Li, G., Ranjith, P., and Fang, L., 2019, An experimental study of mechanical behavior of brittle rock-like specimens with multi-non-persistent joints under uniaxial compression and damage analysis. International Journal of Damage Mechanics, 28, 1490–1522.

Yang, X.X. and Qiao, W.G., 2018, Numerical investigation of the shear behavior of granite materials containing discontinuous joints by utilizing the flat-joint model. Computers and Geotechnics, 104, 69–80.

Yang, Y., Tang, X., Zheng, H., Liu, Q., and He, L., 2016, Three-dimensional fracture propagation with numerical manifold method. Engineering Analysis with Boundary Elements, 72, 65–77.

Yao, W., Cai, Y., Yu, J., Zhou, J., Liu, S., and Tu, B., 2019, Experimental and numerical study on mechanical and cracking behaviors of flawed granite under triaxial compression. Measurement, 145, 573–582.

Yin, Q., Jing, H., and Su, H., 2018, Investigation on mechanical behavior and crack coalescence of sandstone specimens containing fissure-hole combined flaws under uniaxial compression. Geosciences Journal, 22, 825–842.

Zhang, J.Z. and Zhou, X.P., 2020, AE event rate characteristics of flawed granite: from damage stress to ultimate failure. Geophysical Journal International, 222, 795–814.

Zhang, J.Z., Zhou, X.P., Zhou, L.S., and Berto, F., 2019, Progressive failure of brittle rocks with non-isometric flaws: insights from acousto-optic-mechanical (AOM) data. Fatigue and Fracture of Engineering Materials and Structures, 42, 1787–1802.

Zhang, X.P. and Wong, L.N.Y., 2012, Cracking processes in rock-like material containing a single flaw under uniaxial compression: a numerical study based on parallel bonded-particle model approach. Rock Mechanics and Rock Engineering, 45, 711–737.

Zhang, X.P., Liu, Q., Wu, S., and Tang, X., 2015, Crack coalescence between two non-parallel flaws in rock-like material under uniaxial compression. Engineering Geology, 199, 74–90.

Zhang, Z., Wang, D., Ge, X., and Zheng, H., 2016, Three-dimensional element partition method for fracture simulation. International Journal of Geomechanics, 16, 04015074.

Zheng, Q., Liu, E., Yu, D., and Liu, M., 2020, Fatigue and damage properties of non-consecutive jointed mudstone samples subjected to cyclic triaxial loading. Bulletin of Engineering Geology and the Environment, 79, 2467–2481.

Zhou, T. and Zhu, J.B., 2018, Identification of a suitable 3D printing material for mimicking brittle and hard rocks and its brittleness enhancements. Rock Mechanics and Rock Engineering, 51, 765–77.

Zhou, W., Ji, X., Ma, G., and Chen, Y., 2020a, FDEM simulation of rocks with microstructure generated by voronoi grain-based model with particle growth. Rock Mechanics and Rock Engineering, 53, 1909–1921.

Zhou, X.P., Bi, J., Deng, R.S., and Li, B., 2020b, Effects of brittleness on crack behaviors in rock-like materials. Journal of Testing and Evaluation, 48, 2829–2851.

https://doi.org/10.1007/s12303-021-0013-7